This is a preprint of the following article, which is available from http://mdolab.engin.umich.edu
Gustavo L. O. Halila, Guodong Chen, Yayun Shi, Krzysztof J. Fidkowski, Joaquim R. R. A. Martins and Márcio Teixeira de Mendonça. High-Reynolds Number Transitional Flow Simulation via Parabolized Stability Equations with an Adaptive RANS Solver. *Aerospace Science and Technology*, 2019.
The published article may differ from this preprint, and is available by following the DOI: https://doi.org/10.1016/j.ast.2019.05.018.

High-Reynolds Number Transitional Flow Simulation via Parabolized Stability Equations with an Adaptive RANS Solver

Gustavo L. O. Halila, Guodong Chen, Yayun Shi, Krzysztof J. Fidkowski and Joaquim R. R. A. Martins
Department of Aerospace Engineering, University of Michigan, Ann Arbor, MI, 48109

Márcio Teixeira de Mendonça
Instituto de Aeronáutica e Espaço, 12228-904 São José dos Campos, SP, Brazil.

Abstract

The accurate prediction of transition is relevant for aerodynamic analysis and design applications. Extending the laminar flow region over airframes is a potential way to reduce the skin friction drag, which in turn reduces fuel burn and greenhouse gas emissions. This paper introduces a numerical framework that includes the modeling of transition effects for high Reynolds number flows in a high-fidelity, Reynolds–averaged Navier–Stokes (RANS) aerodynamic design framework. The CFD solver uses a discontinuous Galerkin (DG) finite element approach and includes goal-oriented adaptation. The Spalart–Allmaras (SA) turbulence model is used for the closure of the governing equations. In the flow stability analysis, the nonlocal, nonparallel effects that characterize boundary layers are accounted for by using the parabolized stability equations (PSE). Transition onset is obtained through an e^N method based on the PSE computations, while a smooth intermittency function includes the transition region length. Numerical results for the NLF(1)-0416 airfoil present good agreement with experimental data, improving the computations when compared to fully-turbulent ones.

1 Introduction

Transition to turbulence is an important topic in fluid mechanics because it impacts the performance of engineered systems. Viscous drag has a major impact on fuel

efficiency in modern commercial aircraft. Therefore, laminar flows are continuously investigated in the aerospace industry as a tool for increasing overall airplane efficiency, with potential benefits in direct operational costs. In addition, the correct estimation of drag and lift coefficients depends on the accurate computations of the laminar regions in the airframe.

In typical aerospace configurations, different mechanisms are responsible for triggering transition to turbulence. The amplification of unstable Tollmien–Schlichting (TS) waves usually causes transition on wings with low sweep. In the transonic flow regime, wings with high sweep are commonly affected by transition caused by crossflow (CF) vortices. Two types of CF instabilities exist: stationary CF vortices and traveling CF waves. From the physical point of view, these two different families of modes are generated by distinct receptivity mechanisms [1]. While stationary CF vortices are excited by surface variations (surface polishing or suction), traveling CF waves are triggered by an unsteady source, such as freestream turbulence [2]. Only for turbulence levels $Tu > 0.2\%$ and smooth surfaces do the traveling instability waves dominate [3]. Laminar separation bubbles (LSB) may cause transition for separated flows. Reattachment may take place since turbulent boundary layers are more resistant to adverse pressure gradients than laminar ones. Leading-edge attachment line contamination occurs when the fuselage turbulent boundary layer runs onto the leading edge of a swept wing, resulting in the loss of laminar flow over the wing [4]. In addition, attachment line transition takes place if disturbances are amplified in the leading edge region. This happens depending on the flow and leading edge geometry.

In the last few decades, different tools have been proposed to consider transitional flow effects in computational fluid dynamics (CFD). Simplified methods include database methods and analytic criteria. The analytic criteria consider information deduced from experimental data, while simplified methods rely on the disturbance growth computation based on tabulated values or based on analytic relations obtained from exact stability computations that are, in general, performed over self-similar velocity profiles [2]. These simplified methods were first proposed by Gaster and Jiang [5], van Ingen [6], and Stock and Haase [7]. Other examples of database methods are the neural network framework presented by Crouch et al. [8] and the three-parameter database approach used by Drela [9] in a coupled inviscid-viscous flow solver.

Reynolds–Averaged Navier–Stokes (RANS) turbulence models, which are commonly used in engineering applications, are the result of a Favre time-averaging of the original Navier–Stokes equations. As a result, important spectral information is missing [10]. The natural approach to address this shortcoming is to develop an additional model for the transitional region and integrate it into the original turbulence closure. Modeling of transition to turbulence is performed through the inclusion of additional transport equations, generally by adopting an intermittency field. At present, such modified RANS models account for different transition mechanisms, and the specification of boundary conditions for turbulent variables has strong effects on the correct prediction of transitional flows over typical aerospace configurations [11]. A detailed review of RANS-based transition analysis is provided by Pasquale et al. [12].

Large Eddy Simulations (LES) are also used as a tool to study transitional flows. By solving for the large eddies and modeling the small ones, this technique can be used

to model low-Reynolds, transitional flows. At present, LES simulations of airfoils are performed for Reynolds numbers up to $500,000$ [13]. For instance, Uranga et al. [14] performed the simulation of the transitional flow around an airfoil based on the Implicit LES (ILES)approach, using a discontinuous Galerkin (DG) method. Fernandez et al. [13] extended the use of the ILES technique for transitional flows to a hybridized DG (HDG) method and considered flows over aeronautical and compressor cascade airfoils with Reynolds numbers up to $460,000$. As of now, the use of LES is limited to low and moderate Reynolds numbers due its prohibitive computational cost.

Direct Numerical Simulation (DNS) is the highest-fidelity approach in the numerical description of fluid flow. In fact, DNS methods are used to accurately simulate laminar flow breakdown, the development of turbulent spots, and transition to fully-developed turbulent flow [15]. Since eddies down to the Kolmogorov scale must be directly resolved in DNS, stringent requirements are imposed on the mesh size. No additional turbulence modeling or closure assumptions are necessary. As a result, DNS is computationally expensive and, at present, they are not used for industry-relevant aerodynamic configurations.

Stability analysis is a mathematical tool that identifies the growth and decay of certain modes in fluid flows. Unstable amplification of modes leads to instability and the eventual onset of a fully-turbulent state. Typically, the instability of flows to small amplitude perturbations is analyzed using the modal approach [16], and both temporal and spatial problems are considered. The oldest method to characterize boundary layer instabilities is based on the linear Orr–Sommerfeld equation [2] (OSE) and represents a local parallel analysis. This method is usually referred to as Linear Stability Theory (LST), even though there are other linear stability analysis tools that do not consider local and parallel base flows. LST has been widely used to study transition to turbulence; a comprehensive review was performed by Saric [17]. Its main shortcoming is the fact that the boundary layer growth is not considered. Also, nonparallel effects are not included in the formulation.

Nonlocal, nonparallel stability analysis is used to take into account relevant boundary layer flow phenomena. The nonparallel effects relate to the fact that the wall-normal velocity component is nonzero in boundary layers. The inclusion of nonlocal terms represents the convective, history effects in boundary layers. Mathematically, nonlocal effects are related to the presence of streamwise flow derivatives.

Nonparallel effects can be included into the OSE approach, as proposed by Saric and Nayfeh [18] and Crighton and Gaster [19]. The resulting method accounts for nonparallel effects, but the boundary layer history included in the nonlocal terms is not considered. Nonparallel stability methods are based on the Wentzel–Kramers–Brillouin–Jeffreys (WKJB) approximation. This means that the dependent variables can be divided into an amplitude function and an oscillating wave function [20], and that the amplitude is assumed to slowly change in the streamwise direction. The multiple scales (MS) method, described by El–Hady [21], provides a partial differential equation similar to the Parabolized Navier–Stokes equations at some intermediate step, except for additional terms containing frequency and wave numbers [22]. The detailed formulation underlying the MS method can be found in the book by Schmid and Henningson [23]

Another example of a nonlocal, nonparallel flow stability method are the parabolized stability equations (PSE) [22, 24, 25]. These equations allow for the study of the evolution of convectively unstable waves in boundary-layer flows. The PSE method is similar to the MS one, and disturbance growth rates are shown to be very similar when obtained by these two approaches [20]. We select the PSE approach for the present investigation.

Both TS and CF instabilities are considered, and curvature effects can be included in the formulation. The computational cost is of the same order as that of the traditional LST approach [2]. When compared to results obtained by DNS simulations, the neutral curves for incompressible flow over a flat plate produced by PSE computations present close agreement with the higher-fidelity DNS tool results, but at a computational cost that is two orders of magnitude smaller [16].

The possibility of including important physical aspects in the analysis at an affordable computational cost makes the PSE an ideal tool for transition prediction, and some recent studies highlight the relevance of using PSE for transition analysis over general aerospace configurations [26]. A complete review of the use of stability analysis tools for transition prediction is provided by Arnal [27]. For transition purposes, the use of linear tools that consider infinitesimally small disturbance amplitudes is an efficient approach.

By using the PSE method, growth rates are obtained for disturbances superimposed on a given base flow. The growth rate integration leads to an N-factor that is then used to predict the transition region onset, as first proposed by van Ingen [28]. A smooth, continuous intermittency function is used to estimate the transition region extent. The resulting information for the transition front and transition length is then used to select regions of laminar and turbulent flow within a RANS framework.

In contrast to other efforts that used an ILES approach to handle transitional flows with a DG method, our approach targets high Reynolds numbers, which is required to model large aircraft. In addition, the computational cost of our approach is much lower than ILES.

While the ILES approach in a DG framework [13, 14] benefits from the low numerical dissipation that high-order discretization schemes present and that are relevant for applications involving transition to turbulence, it is not compatible with realistic aerodynamic problems because the Reynolds numbers are moderate at best. By using the PSE technique along with a high-order RANS implementation, we include an accurate prediction of the physics of transition, considering both nonlocal and nonparallel effects that are representative of boundary layer flows, while retaining the benefits of a high-order CFD approach. In our approach, the computational costs for high Reynolds number, transitional flow simulations are of the same order of magnitude of those of a fully turbulent RANS run and, therefore, are compatible with industry requirements. The goal-oriented mesh adaptation can be based on a drag objective function, which is a relevant aerodynamic metric for design purposes. The combination of these elements makes our approach well-adapted for studying realistic aerospace flows with the inclusion of transition to turbulence. We present results for the NLF(1)-0416 airfoil, for which a vast amount of experimental data is available [29], and show that including transition to turbulence in the computations improves agreement with experimental

data.

This paper is organized as follows. Section 2 presents the governing equations and the fundamentals behind the discontinuous Galerkin finite-element method and introduces the techniques used for mesh adaptation and error estimation. The modal stability analysis approach is also introduced in this section, and an in-depth discussion of the PSE approach is included. Section 3 focuses on the transition prediction methods, including the e^N methodology, the required modifications in the underlying RANS model to account for transition, and the coupling between the transition module and the CFD solver. Our compressible PSE approach is verified in Sec. 4 and the numerical results from the coupled PSE-CFD approach are presented in Sec. 5. We end with the conclusions in Sec. 6.

2 Governing Equations and Discretization

Our transition prediction framework is based on a PSE flow stability tool coupled to a CFD solver. A boundary layer solver provides the base flow information required for the stability computations, and our LST implementation, coupled to a database method, indicates the wave modes that should be used in the PSE computation. The results from this flow stability solve are then sent to the CFD solver, and the underlying Spalart–Allmaras (SA) turbulence model is adapted to include transition to turbulence effects. The details of the transition module are provided in Sec. 3. Section 2.1 introduces the principles behind the discontinuous Galerkin approach, while Section 2.2 presents the error estimation and mesh estimations algorithms used in this paper. Section 2.3 is an overview of the modal stability analysis approach that comprises both LST and PSE techniques. We introduce the PSE formulation in Section 2.4.

2.1 Discontinuous Galerkin Finite-Element Method

The equations governing the fluid flow system in this work are written in conservative form as

$$\frac{\partial \mathbf{u}}{\partial t} + \nabla \cdot \vec{\mathbf{F}}(\mathbf{u}, \nabla \mathbf{u}) + \mathbf{S}(\mathbf{u}, \nabla \mathbf{u}) = \mathbf{0}, \tag{1}$$

where $\mathbf{u}$ is the conservative state vector composed of the flow variables, $\vec{\mathbf{F}}$ denotes the total inviscid and viscous flux vectors, and $\mathbf{S}$ represents the source term required when modeling turbulence. When running Reynolds–averaged turbulent cases, we use the Spalart–Allmaras (SA) one-equation model, with a negative turbulent-viscosity modification [30].

We discretize Eq. (1) with the discontinuous Galerkin (DG) finite-element method, which is suitable for high-order accuracy and *hp*-refinement [31–33]. The computational domain Ω is divided into a shape-regular mesh $\mathcal{T}_h$ consisting of N_e non-overlapping elements Ω_e, $\mathcal{T}_h = \{\Omega_e : \bigcup_{e=1}^{Ne} \Omega_e = \Omega, \bigcap_{e=1}^{Ne} \Omega_e = \emptyset\}$. In DG, the state components are approximated by piece-wise polynomials in the approximation space $\mathcal{V}_h^p$, with no continuity constraints imposed on the approximations between adjacent elements. The approximation space consists of element-wise polynomials and is defined as $\mathcal{V}_h^p = \{v_h \in L^2(\Omega) : v_h|_{\Omega_e} \in \mathcal{P}^{p_e}, \forall \Omega_e \in \mathcal{T}_h\}$, where $\mathcal{P}^{p_e}$ denotes polynomials of order p_e on element

Ω_e, a distribution that is not necessary uniform throughout the mesh. The weak form of Eq. (1) is obtained by multiplying the equation by test functions (taken from the approximation space), integrating by parts, and coupling elements via unique inter-element fluxes. We use the Roe approximate Riemann solver [34] for the inviscid flux, and the second form of Bassi and Rebay (BR2) for the viscous flux [35]. Choosing a basis for the test and trial spaces yields a system of nonlinear, algebraic equations,

$$\mathbf{R}_H(\mathbf{U}_H) = \mathbf{0}, \tag{2}$$

where $\mathbf{R}_H$ is the discrete residual vector that is a nonlinear function of the discrete state vector, $\mathbf{U}_H$. For the steady-state problems considered in this work, $\mathbf{R}_H$ is the discrete spatial residual vector. The subscript H refers to the discretization fidelity of the approximation or test space with respect to the approximation order and mesh refinement.

2.2 Error Estimation and Mesh Adaptation

The advantages of high-order DG methods can be best realized with *hp*-adaptation using appropriate adaptation strategies [36]. In aerospace applications, we usually care primarily about integrated forces such as lift or drag, instead of the accurate state solution everywhere over the computational domain. Adjoint-based techniques, which have been studied in depth and successfully demonstrated in aerospace engineering problems [37–39], are able to estimate the output error and provide local indicators for adaptation.

Consider a scalar output of interest that is a functional of the flow states, $\mathcal{J}(\mathbf{u})$. The error in the output due to finite dimensional discretization space can be defined as $\mathscr{E} \equiv J_H(\mathbf{U}_H) - \mathcal{J}(\mathbf{u})$. In practice, the difference between the outputs calculated with the discrete state solution on the coarse space (subscript H) and a finer space (subscript h), i.e., $J_H(\mathbf{U}_H) - J_h(\mathbf{U}_h)$, serves as a surrogate to the "true" error. In the present work, the fine space is achieved by an increment of one on the elements' approximation order, i.e., $p_e + 1$. Instead of solving the flow problem in the fine space, we use the linear adjoint solution on the fine space $\mathbf{\Psi}_h$, defined as the output sensitivity to the residual perturbation

$$\left(\frac{\partial \mathbf{R}_h}{\partial \mathbf{U}_h}\right)^T \mathbf{\Psi}_h + \left(\frac{\partial J_h}{\partial \mathbf{U}_h}\right)^T = \mathbf{0}. \tag{3}$$

Then, the output error can be estimated using an adjoint-weighted residual,

$$\begin{aligned} \mathscr{E} \approx \delta J &= J_H(\mathbf{U}_H) - J_h(\mathbf{U}_h), \\ &= J_h(\mathbf{U}_h^H) - J_h(\mathbf{U}_h) \approx \frac{\partial J_h}{\partial \mathbf{U}} \delta \mathbf{U}, \\ &= -\mathbf{\Psi}_h^T \delta \mathbf{R}_h = -\mathbf{\Psi}_h^T \mathbf{R}_h(\mathbf{U}_h^H), \end{aligned} \tag{4}$$

where $\mathbf{U}_h^H$ is the state injected into the fine space from the coarse space, which generally does not give a zero fine space residual, $\mathbf{R}(\mathbf{U}_h^H) \neq \mathbf{R}_h(\mathbf{U}_h) = \mathbf{0}$. The error estimates

given by Eq. (4) can be localized to each element and serve as an indicator to drive the mesh adaptation,

$$\mathcal{E} = -\boldsymbol{\Psi}_h^T \mathbf{R}_h(\mathbf{U}_h^H) = -\sum_{e=1}^{N_e} \boldsymbol{\Psi}_{h,e}^T \mathbf{R}_{h,e}(\mathbf{U}_h^H), \qquad \epsilon_e = |-\boldsymbol{\Psi}_{h,e}^T \mathbf{R}_{h,e}(\mathbf{U}_h^H)|, \tag{5}$$

where $\mathcal{E}$ represents the total output error estimate and ϵ_e denotes the localized error indicator for element Ω_e.

To capture the highly anisotropic physics in the boundary layer with moderate degrees of freedom (DOF), we use unstructured mesh optimization through error sampling and synthesis (MOESS) [40]. In MOESS, the optimal mesh, encoded with a continuous metric field, is iteratively determined by equally distributing the marginal error-to-cost ratio of local refinement. This process requires models indicating how the error and cost change as the metric field changes. The cost of refinement measured with DOF can be directly related to the local metric if a fixed approximation order is used. On the other hand, the error model is obtained with a local sampling approach to determine an empirical form of output convergence,

$$\epsilon_e = \epsilon_{e,0} \exp[\mathrm{tr}(\mathcal{R}_e \mathcal{S}_e)], \tag{6}$$

where $\mathcal{R}_e$ is a symmetric error convergence tensor containing the directional convergence information, and $\mathcal{S}_e$ is the proposed metric step matrix encoding both the shape and the size changes of the element e. In the sampling, we prescribe several refinement options indexed by i, with different step matrix $\mathcal{S}_{e,i}$.

Figure 1 shows four refinement options for a triangular element. For each refinement option i, the corresponding error estimate $\epsilon_{e,i}$ is used to determine the rate tensor $\mathcal{R}_e$ using Eq. (6). The error estimates require the fine space adjoint solution for each proposed refinement, which can be expensive to solve even for a local patch of elements. Instead, we use an element-local projection method [41] to approximate the fine-space adjoint in semi-refined spaces associated with each refinement option. With the cost and error models, one can obtain the local marginal error-to-cost ratio. MOESS then follows an iterative process to equidistribute the marginal error-to-cost ratio at a given target cost level [40].

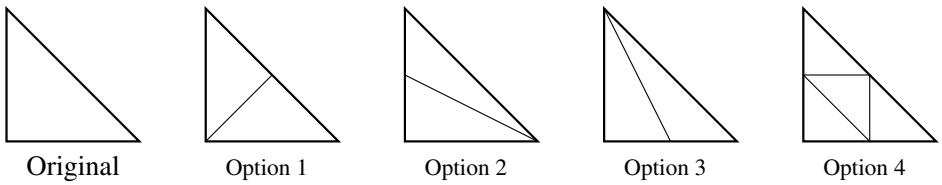

Figure 1: Four refinement options for a triangle. Each one is implicitly considered during the error sampling, although the elements are never actually refined.

2.3 Modal Linear Stability Theory

In modal linear stability theory, the stability problem is solved by using a set of wave modes, each of which is solved independently. Both PSE and LST are examples of modal linear stability methods.

The overall principle is based on the decomposition of any flow property $\mathbf{q}$ into a steady base state $\bar{\mathbf{q}}$ and an unsteady perturbation component, $\tilde{\mathbf{q}}$, as follows:

$$\mathbf{q}(\mathbf{x}, t) = \bar{\mathbf{q}}(\mathbf{x}) + \epsilon\tilde{\mathbf{q}}(\mathbf{x}, t), \tag{7}$$

where $\mathbf{x}$ is the space coordinate vector, t is the time, and $\mathbf{q} = (\rho, u, v, w, T)$ is the flow state vector. As long as we consider the linear stability problem, the perturbations have small amplitudes such that $\epsilon \ll 1$. When such an *ansatz* is applied to the Navier–Stokes equations, a linearization is performed by neglecting terms of $\mathcal{O}(\epsilon^2)$ and $\mathcal{O}(\epsilon^3)$. The equations for the steady flow, that also satisfy the Navier–Stokes equations, are subtracted, and we obtain the linearized Navier–Stokes equations (LNSE), which are written as an initial value problem. If the base flow $\bar{\mathbf{q}}$ is steady, time and space dependencies are split in this equation. A Fourier decomposition in time can be introduced using $\tilde{\mathbf{q}} = \hat{\mathbf{q}}\exp(-i\omega t)$, where ω is the angular frequency. The linearization introduced in the Navier–Stokes equations leading to the LNSE is only valid when the disturbance amplitude remains small such that the nonlinear terms are negligible. Indeed, the real nonlinear system might present an unstable behavior if finite-amplitude disturbances are considered, under conditions in which the linearized system remains stable.

In modal linear stability analysis, the perturbation term is written as the product of an amplitude $\hat{\mathbf{q}}$ and a phase function Θ:

$$\tilde{\mathbf{q}} = \hat{\mathbf{q}}e^{i\Theta}. \tag{8}$$

Different stability methods are based on distinct assumptions regarding the topology of the base flow $\bar{\mathbf{q}}$ and the fluctuation $\tilde{\mathbf{q}}$. The overall differences between LST (Orr–Sommerfeld) and PSE methodologies are detailed in Table 1, where $\alpha = 2\pi/L_x$ is the streamwise wave number, $\beta = 2\pi/L_z$ is the spanwise wave number, with L_x and L_z the wavelengths in the streamwise (x) and spanwise (z) directions, respectively. Also, ω is the angular frequency, and x^* represents the base flow slow variation properties in the streamwise direction. The wall-normal direction is denoted by y.

Table 1: Classification of stability analysis theory [16].

Method	Assumption	Base flow	Amplitude function	Phase function Θ
PSE	$\partial_x\bar{\mathbf{q}} \ll \partial_y\bar{\mathbf{q}}; \partial_z\bar{\mathbf{q}} = 0$	$\bar{\mathbf{q}}(x^*, y)$	$\hat{\mathbf{q}}(x^*, y)$	$\int \alpha(x')dx' + (\beta z - \omega t)$
LST	$\partial_x\bar{\mathbf{q}} = \partial_z\bar{\mathbf{q}} = 0$	$\bar{\mathbf{q}}(y)$	$\hat{\mathbf{q}}(y)$	$\alpha x + (\beta z - \omega t)$

The first flow stability studies focused on flows in which inhomogenity is observed in only one spatial direction. This is the case of a channel flow in which the base flow only presents variations in the wall-normal direction. In this specific case, $\partial_x\bar{\mathbf{q}} = \partial_z\bar{\mathbf{q}} = \mathbf{0}$, and $\bar{\mathbf{q}}(\mathbf{x}) = \bar{\mathbf{q}}(y)$. Such approximations are valid for parallel flows, such as Couette and Pouiseuille flows [42]. The introduction of a Fourier decomposition along the streamwise (x) and the spanwise (z) directions may be written to derive different variations of the Orr–Sommerfeld equations [23].

Boundary-layer flows are characterized by two inhomogeneous spatial directions, with the base flow depending both on streamwise and normal coordinates, with slow

variations in the streamwise direction, i.e., $\partial_x \bar{\mathbf{q}} \ll \partial_y \bar{\mathbf{q}}$. To solve such a type of flow, the parabolized stability equations (PSE) method was first introduced by Bertolotti and Herbert [24]. In contrast to the eigenvalue problem in the Orr–Sommerfeld equations, the PSE technique solves the stability problem by integrating the LNSE via a marching procedure along the streamwise direction. The initial values for the eigenfunctions $\hat{\mathbf{q}}$ and the streamwise wavenumber (α) are obtained from a local stability analysis performed in the first streamwise station. Bertolotti [43] and Herbert [22] published comprehensive reviews on the PSE method.

2.4 PSE Theoretical Formulation

The PSE method represents base flows in which variations in the streamwise direction are much smaller than those in the wall-normal direction. Mathematically, this is expressed as

$$\partial_x \bar{\mathbf{q}} \ll \partial_y \bar{\mathbf{q}}; \quad \partial_z \bar{\mathbf{q}} = \mathbf{0}, \tag{9}$$

$$\bar{\mathbf{q}}(\mathbf{x}) = \bar{\mathbf{q}}(x^*, y), \tag{10}$$

where x^* is a scaled version of x used to represent the base flow slow variation in the x direction. From the base flow assumptions, it follows that the PSE method is well-adapted to the prediction of flows such as boundary layers, jets, wakes, and mixing layers at high Reynolds numbers. The PSE methodology is valid for convectively unstable flows.

The base flow velocity components $\bar{u}$ and $\bar{v}$, aligned with the streamwise and spanwise directions, respectively, exhibit small variations in the streamwise (x) direction and are constant along the spanwise (z) direction. We introduce the local Reynolds number, $Re = U_e \delta(x)/\nu$ where ν is the kinematic viscosity and $\delta(x)$ is a characteristic length scale proportional to the boundary layer thickness, $\delta(x) = \sqrt{\nu x/U_e}$, where U_e is the unperturbed boundary layer edge velocity. The wall-normal component, $\bar{w}$, is nonzero and scales with $1/Re$. Formally defining the slowly varying scale $x^* = x/Re$, the scalings are:

$$\begin{aligned} \bar{w} &\sim \frac{1}{Re}, \\ \frac{\partial}{\partial x^*} &\sim \frac{1}{Re}, \\ \alpha &= \alpha\left(x^*\right), \\ \hat{\mathbf{q}} &= \hat{\mathbf{q}}\left(x^*, y\right). \end{aligned} \tag{11}$$

The perturbation vector is expanded in terms of its truncated Fourier components assuming time-periodicity,

$$\tilde{\mathbf{q}}(x, y, x, t) = \sum_{m=-M}^{M} \sum_{n=-N}^{N} \breve{\mathbf{q}}_{m,n}(x, y) \exp\left[i\left(m\beta z - n\omega t\right)\right], \tag{12}$$

where $\breve{\mathbf{q}}$ represents the fast varying wave function with a slowly-varying amplitude $\hat{\mathbf{q}}(x, y)$:

$$\breve{\mathbf{q}}_{m,n}(x, y) = \hat{\mathbf{q}}_{m,n}(x, y) \exp\left[i \int_x \alpha_n (x')\, dx'\right], \tag{13}$$

and $\hat{\mathbf{q}}(x, y)$ has a slow variation in x.

If a linear approach is considered, only one mode for each spanwise direction and time is needed. Using the PSE approximation, the streamwise derivatives of the amplitude $\breve{\mathbf{q}}$ are

$$\frac{\partial \breve{\mathbf{q}}}{\partial x} = \left(i\alpha\hat{\mathbf{q}} + \frac{\partial \hat{\mathbf{q}}}{\partial x}\right) \exp\left[i \int_x \alpha (x')\, dx'\right], \tag{14}$$

$$\frac{\partial^2 \breve{\mathbf{q}}}{\partial x^2} = \left(-\alpha^2\hat{\mathbf{q}} + 2i\alpha\frac{\partial \hat{\mathbf{q}}}{\partial x} + i\frac{d\alpha}{dx}\hat{\mathbf{q}}\right) \exp\left[i \int_x \alpha (x')\, dx'\right]. \tag{15}$$

To obtain the linear PSE equations, we replace Eqns. (13), (14), and (15) in the LNSE and neglect terms of $\mathcal{O}(\epsilon^2)$. We also consider the scaling from Eq. (11) and neglect higher derivatives with respect to x in the viscous terms (noting that $\frac{\partial}{\partial x}\frac{1}{Re} \sim \epsilon^2$). The resulting linear PSE equations in compact form are

$$\mathbf{A}\hat{\mathbf{q}} + \mathbf{B}\frac{1}{h_y}\frac{\partial \hat{\mathbf{q}}}{\partial y} + \mathbf{C}\frac{1}{h_y^2}\frac{\partial^2 \hat{\mathbf{q}}}{\partial y^2} + \mathbf{D}\frac{1}{h_x}\frac{\partial \hat{\mathbf{q}}}{\partial x} = \mathbf{0}, \tag{16}$$

where h_x and h_y are curvature metrics. The entries for the compressible PSE operators $\mathbf{A}$, $\mathbf{B}$, $\mathbf{C}$, and $\mathbf{D}$ are detailed by Hanifi et al. [20]. The boundary conditions are:

$$\hat{u} = \hat{v} = \hat{w} = \hat{T} = 0 \quad \text{at} \quad y = 0, \tag{17}$$

$$\hat{u} = \hat{v} = \hat{w} = \hat{T} \to \infty \quad \text{as} \quad y \to \infty. \tag{18}$$

In the PSE framework, changes in amplitude along the slow spatial direction are contained both in the amplitude function $\hat{\mathbf{q}}$ and in the phase function defined in Eq. (13). To remove such ambiguity, a normalization condition is required. One possibility for the normalization is imposing

$$\int_0^\infty \hat{\mathbf{u}}^\dagger \frac{\partial \hat{\mathbf{u}}}{\partial x} dy = 0, \tag{19}$$

where the superscript † represents the complex conjugate. By using this normalization condition, we force the fast disturbance variations in the streamwise direction (x) to be absorbed into the phase function. This also ensures that the scaling of $(1/Re)$ in $\partial\hat{\mathbf{q}}/\partial x$ is valid.

The physical growth of an arbitrary disturbance ξ is defined as

$$\sigma = \frac{1}{h_x}\left(-\alpha_i + \Re\left[\frac{1}{\xi}\frac{\partial \xi}{\partial x}\right]\right), \tag{20}$$

where the subscript i indicates the imaginary part. The disturbance kinetic energy is used to measure the disturbance growth,

$$E(x) = \int_0^\infty \left(|\hat{\mathbf{u}}|^2 + |\hat{\mathbf{v}}|^2 + |\hat{\mathbf{w}}|^2\right) dy, \tag{21}$$

and, hence, Eq. (20) becomes:

$$\sigma_E = \frac{1}{h_x}\left(-\alpha_i + \frac{1}{2}\frac{d}{dx}\ln\left[E(x)\right]\right). \tag{22}$$

The linear PSE equations (16) are intended to be parabolic. Therefore, it is possible to treat the streamwise direction as a pseudo-time and then to implement a marching strategy in this spatial direction. Numerical instabilities appear when the streamwise integration step is too small [16]. The reason for that, as explained by Herbert [22], is that there are traces of ellipticity that inject ill-posed characteristics. One remedy for this is the use of a first-order backward difference scheme with a lower integration step limit $\Delta x > 1/|\alpha_r|$. To relax this limit, Andersson et al. [44] propose a stabilization procedure leading to $\Delta x > 1/|\alpha_r| - 2s$, where s is a small number.

Due to the predominantly parabolic character of the linear PSE equations (16), the disturbance evolution is influenced by both local and upstream flow conditions. Therefore, the parabolized stability equations are recognized as a *nonlocal* method, in contrast to, for instance, the Orr–Sommerfeld equation that is a *local* approach. For three-dimensional flows, there are some possibilities for the marching direction. Using an orthogonal coordinate system, the most common approach is to orient the streamwise direction towards a normal to the leading edge, where the spanwise direction is parallel to the leading edge. Another choice would be perform a marching that follows the inviscid streamline. A complete discussion on suitable marching directions is available in the literature [26, 45]. Another relevant aspect to be considered when using PSE is the starting integration point. It is necessary to place this point some flow stations upstream of the neutral point location. Langlois et al. [46] discusses this issue in more depth.

3 Transition Prediction

3.1 N-factor and Transition Region Beginning

The beginning of the transition region is determined based on an e^N method. The amplification factor, or N-factor, is defined as

$$N = \ln\left(\frac{A}{A_0}\right) = \int_{x_0}^{x} \sigma_E\left(x'\right) dx', \tag{23}$$

where A_0 is the disturbance amplitude at the first neutral-stability point. The N-factor envelope is obtained by running the PSE code using different frequencies and spanwise wave numbers, and superimposing the resulting N-factor curves at each station during the PSE solution.

The position in which the transition region starts, $x_{TR,\mathrm{beg}}$, is allowed to be in between two cells by using a simple linear interpolation that considers the two mesh points in between which the N-factor envelope satisfies the threshold value for the amplification factor, usually called critical amplification,or critical N-factor. This leads

to the following expression for the transition location,

$$x_{TR,\mathrm{beg}} = \frac{(N_R - N_{crit})\, x_L + (N_{crit} - N_L)\, x_R}{(N_R - N_{crit}) + (N_{crit} - N_L)}, \tag{24}$$

where x_L and x_R are, respectively, the left and right neighbors of the position where N_{crit} is reached and N_L and N_R are the corresponding N-factor values.

The critical value for the N-factor, N_{crit}, is obtained from experimental data. For some transition mechanisms, empirical correlations are available. For Tollmein–Schlichting waves, Mack [47] suggested correlating the critical N-factor to the turbulence level, Tu, using

$$N_{\mathrm{crit,TS}} = -8.43 - 2.4 \ln(Tu)\,. \tag{25}$$

This correlation is valid for $0.001 < Tu < 0.01$, and sometimes is also used to indicate critical values for crossflow (CF) vortices [26].

Since flow stability tools only provide the transition region starting point (transition onset), additional correlations are used to estimate the length of the transition region. Our framework also includes correlations that allow for the prediction of transition triggered by flow separation through laminar separation bubbles (LSB) and leading edge transition and contamination, as discussed by Shi et al. [48].

3.2 Intermittency Function and Interaction with the Spalart–Allmaras Turbulence Model

Physically, the intermittency indicates the probability of a flow location to be turbulent. We use a smooth intermittency function to generate the transition region in a RANS computation framework, i.e.,

$$\gamma = 1 - \exp^{-0.413\xi^2}, \tag{26}$$

where

$$\xi = \frac{3.36\left(s - s_{tr}^{\mathrm{beg}}\right)}{\left(s_{tr}^{\mathrm{end}} - s_{tr}^{\mathrm{beg}}\right)}, \tag{27}$$

where s is the arc length measured from the stagnation point and the superscripts beg and end refer to the beginning and end of the transition region, respectively. The ending arc point, s_{tr}^{end}, is determined based on the correlation [49],

$$s_{tr}^{\mathrm{end}} = 2.3\sqrt{\frac{U_e}{\nu_e}}\,(\delta_1)^{1.5} + s_{tr}^{\mathrm{beg}}, \tag{28}$$

where U_e and ν_e are the velocity and kinematic viscosity at the boundary layer edge, respectively, and δ_1 is the boundary layer displacement thickness. All these quantities are evaluated at the flow position corresponding to s_{tr}^{beg}.

The intermittency function γ is used as a factor of both production and destruction terms in the SA turbulence model such that the eddy viscosity production is suppressed

in laminar regions [50]. The governing equation for the SA model working variable, $\tilde{\nu}$, is then modified to [30]

$$\frac{D\tilde{\nu}}{Dt} = \gamma P - \gamma_{\text{lim}} D + T + \frac{1}{\sigma}\left[\nabla \cdot \left(\left(\nu + \tilde{\nu}\right)\nabla\tilde{\nu}\right) + c_{b2}\left(\nabla\tilde{\nu}\right)^2\right], \tag{29}$$

where P and D are, respectively, the production and destruction terms and [51]

$$\gamma_{\text{lim}} = \min\left[\max\left(\gamma, 0.1\right), 1.0\right]. \tag{30}$$

Allmaras and Johnson [30] describe the other variables in Eq. (29) in more detail.

3.3 Transition Module Coupling with CFD Solver

The interaction between the CFD and the transition module, which can perform both LST and PSE analyses, is illustrated in Fig. 2. Our conical boundary layer code is used to provide the laminar flow field given a pressure coefficient (C_p) distribution.

The C_p distribution can be obtained from the initial fully-turbulent RANS simulation. Another possibility, adopted in this work, is to consider the C_p distribution from a lower-fidelity flow solver. We use Xfoil [52] to provide the initial C_p distribution. As Xfoil uses a panel approach that includes viscous corrections and transition estimation; we can use its C_p distribution as a direct boundary condition for the boundary layer solver. Since an initial transition location in a lower fidelity environment is taken into account and reflected in the C_p distribution, no iteration is needed in the process. This is especially valid for flows where no shock waves are present, such that the C_p distribution is not significantly affected by the transition location, as will be illustrated in Sec. 5. For a three-dimensional extension of the approach we propose here, the pressure coefficient extraction from the RANS field is performed through slices at selected spanwise stations normal to the leading edge. This approach is the one used in a previous work involving LST computations [48]. No further modifications in the PSE tool are needed, as our formulation is *quasi*-3-D.

It is also possible to extract the base flow from the CFD solver itself. This second approach, which is not used in this paper, is able to consider separated flow regions [53], but involves placing more points inside the boundary layer region in the CFD computation, which increases its computational cost compared to a boundary layer solver.

A set of suitable waves is then provided by our LST code. These waves, along with base flow information, are provided to the PSE, which computes the transition onset point. The intermittency function (26) is then prescribed to all mesh elements such that the turbulence model considers laminar, transitional, and turbulent regions. The transition prediction framework is illustrated in Fig. 2.

With the pressure coefficient distribution, geometry, and simulation conditions, we trigger the laminar boundary layer solution and output the required base flow information. An e^N method based on the PSE N-factor calculations is then used to provide the transition location. We calculate the intermittency function and perform the required modifications in the underlying RANS model as we detail in section 3.2.

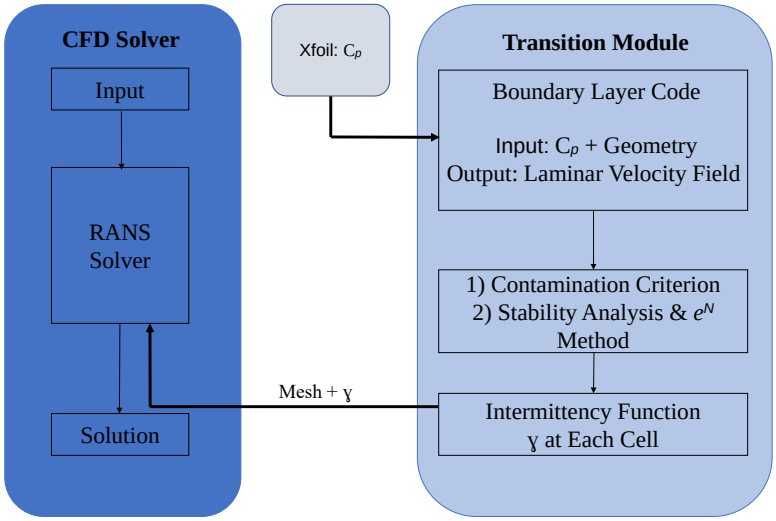

Figure 2: Transition prediction framework (adapted from [48]).

4 PSE Verification

Our compressible PSE tool is able to advance the PSE solution using both first and second-order implicit schemes and considers 2-D and quasi 3-D base flows with uniform or nonuniform meshes. The stabilization procedure suggested by Andersson et al. [44] is also included in the implementation. A growing mesh that emulates the boundary layer growth is included as an option. The normal to the wall direction is discretized using a spectral method based on the Chebyshev collocation points with a suitable mapping to the computational domain and point clustering close to the wall and boundary layer edge for high-speed flows. The curvature metrics highlighted in Sec. 2.4 are also included in the current implementation. Curvature effects are also introduced in the base flow quantities inside the PSE operators. The first streamwise position is solved using a local method based on the PSE operators without the nonparallel terms. The resulting eigenfunctions are then used as starting values for the PSE marching.

4.1 Subsonic and Supersonic Flat Plate Test Cases

To verify the compressible PSE solver (StabFlow), two flat plate test cases are performed corresponding to low and high Mach number flows. In both cases, we compared results to those obtained with the NOLOT code, which is a linear compressible PSE implementation [20].

For the low Mach number test case, we select a constant, dimensionless reduced frequency $F = 1.4 \times 10^{-4}$. The reduced frequency is related to the dimensional frequency, f, according to $F = 2\pi f\,(\nu/U_e^2)$. The Mach number is 0.01 and the marching ranges from $Re_\delta = 100$ to $Re_\delta = 650$, where Re_δ is the Reynolds number based on the Blasius characteristic length variable. The freestream temperature is 299 K and the Prandtl number is 0.71. For this test case, the waves are aligned with the streamwise direction ($\beta = 0$). For this simulation, 60 Chebyshev points are used in the wall-normal

direction. The results for the energy-based growth rate, σ_E, are shown in Fig. 3. The agreement between the benchmark code (NOLOT) and our implementation (StabFlow) is good for both growing and rectangular meshes, with a local error that within 5% after the initial transient behavior vanishes.

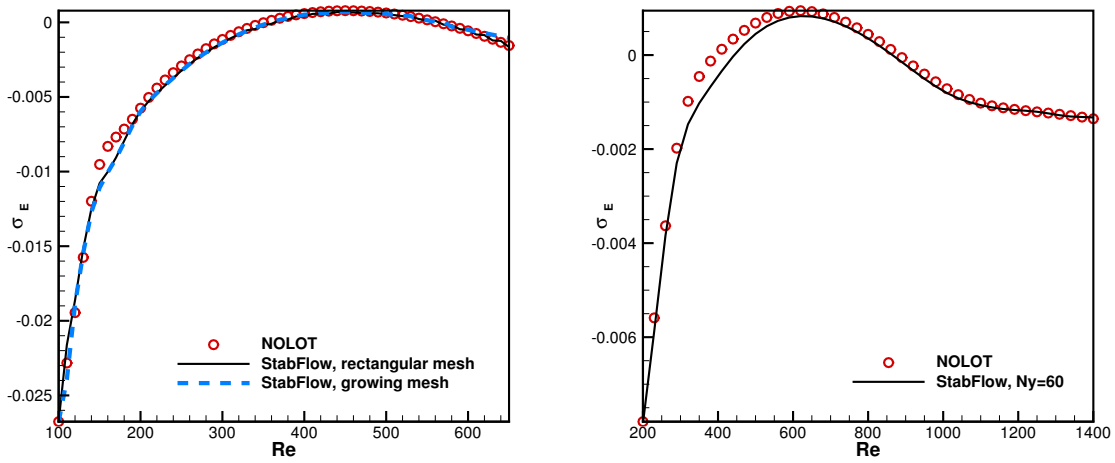

(a) $M = 0.01$ (b) $M = 1.6$

Figure 3: Energy-based growth rates for subsonic (left) and supersonic (right) flow over a flat plate.

A numerical simulation considering supersonic flow at $M = 1.6$ over a flat plate is also considered at $T = 300$ K and $Pr = 0.71$. For this specific test case, we choose an oblique wave with $\beta/R = 1.52 \times 10^{-4}$ and a reduced frequency $F = 5.0025 \times 10^{-5}$. The marching extends from $Re_\delta = 200$ to $Re_\delta = 1400$ with a step of $\Delta Re_\delta = 30$. The simulation is converged for 60 Chebyshev points in the wall-normal direction. The results for the energy-based growth rate, σ_E, are shown in Fig. 3. Once again, the results are in good agreement with the NOLOT data. Some transient effects appear in the early marching stations, but vanish afterwards.

To inspect the eigenfunctions, we plot the wave amplitudes for the three velocity components, temperature, and density at the marching mid-station in Fig. 4. The wall-normal perturbation velocity decay is the one that requires a larger computational domain, as shown in Fig. 4. For this reason, the computational domain should be as large as 100 to 200 times the local reference length at each marching station if TS waves are included. Crossflow instabilities decay faster in the freestream and a smaller computational domain is considered.

4.2 NACA 0012 Airfoil

To further investigate our PSE implementation with transition prediction, we use a NACA 0012 airfoil at a zero angle of attack, $M = 0.1$, and chord-based Reynolds number of 1, 3, 5, 8, and 15 million. The base flows used here are obtained from our conical boundary layer code. The C_p distribution from an initially fully turbulent run

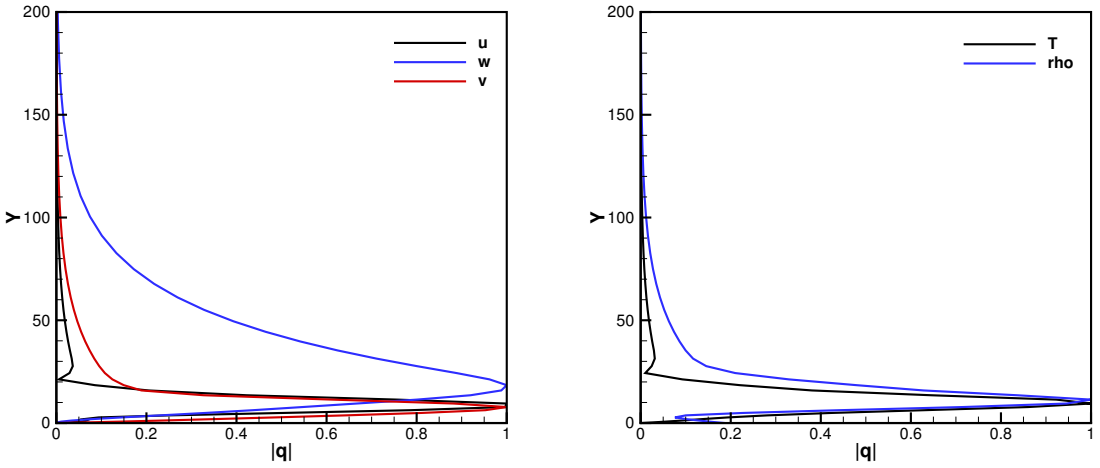

(a) Perturbation velocity

(b) Perturbation temperature and density

Figure 4: Normalized absolute values of eigenfunctions in the mid-station for flow at $M = 1.6$ over a flat plate.

is used as the boundary condition for the boundary layer solver.

Since there are no experimental results for this specific case, we compare our results to those obtained with our LST model, which was extensively validated against experimental data by Shi et al. [48, 54]. This is an appropriate test case since TS waves are not significantly affected by curvature, nonlocal, and nonparallel effects, which are not accounted for in the LST formulation.

Figure 5 shows the N-factor envelopes for all the considered Reynolds numbers, together with the critical N-factor, $N_{\text{crit},TS} = 8.14$. This critical N-factor was obtained by using Eq. (25) for a turbulence level of $Tu = 0.1\%$. This figure also shows the beginning and end chord locations for the transition region for all five flight conditions. Since the NACA 0012 airfoil is symmetric and we use a zero angle of attack, we only display results for the airfoil suction side. We observe that, with increasing freestream Reynolds number, the transition front moves upstream and the transition region becomes shorter than for smaller freestream Reynolds numbers, indicating that the model is able to reproduce the fact that, for higher Reynolds numbers, the flow structures evolution that lead to turbulent flow is faster than for lower Reynolds flows.

The results for the transition region starting location for the NACA 0012 test cases are listed in Table 2. Agreement between both flow stability analysis implementations is good, and the average error is of 0.73% across all the Reynolds numbers tested, with a maximum error of 1.11% for $Re = 8 \times 10^6$.

4.3 NLF(1)-0416 Airfoil

The Natural Laminar Flow NLF(1)-0416 airfoil is a general aviation airfoil largely tested at the NASA Langley Low-Turbulence Pressure Tunnel [29]. Turbulence intensity measurements in this wind tunnel indicate that it is a quiet test apparatus [55].

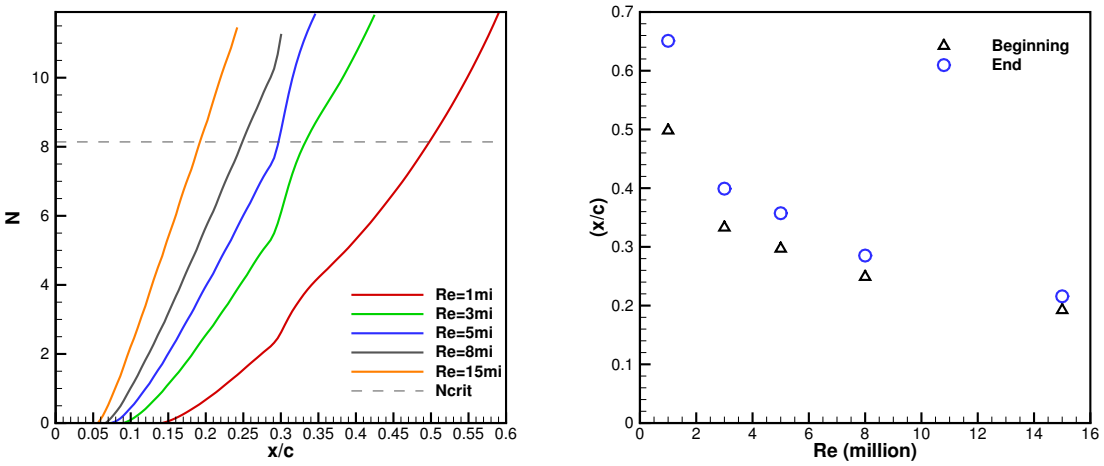

(a) N-factor envelopes (b) Transition location

Figure 5: N-factor envelopes (left) and transition locations (right) for a NACA 0012 airfoil at multiple Reynolds numbers.

Table 2: NACA 0012 airfoil transition region starting locations for different Reynolds numbers.

Re (million)	PSE, $(x/c)_{tr}$	LST, $(x/c)_{tr}$	Difference (%)
1	0.498	0.493	0.87
3	0.333	0.349	0.74
5	0.297	0.296	0.39
8	0.249	0.246	1.11
15	0.192	0.191	0.56

However, Coder [50] mentions that the original turbulence intensities for this wind tunnel might not lead to good agreement with experimental data when used along with transition modeling tools. Therefore, we choose $Tu = 0.1\%$ for this test case. As a result, the critical N-factor is $N_{\text{crit,TS}} = 8.14$ as suggested by Eq. (25).

We select two flight conditions, depicted in Table 3. According to Somers [29], transition is triggered by amplification of TS waves in the airfoil suction side for both of these flight conditions.

Table 3: NLF(1)-0416 flight conditions.

Condition	Re (million)	M	Angle of attack (degrees)
1	4	0.1	0
2	2	0.1	4

For flight condition 1, our transition prediction framework considers a set of TS waves with frequencies ranging from 1100 to 2400 Hz for the airfoil suction side, and from 580 to 2000 Hz for the pressure side. For flight condition 2, the frequencies range

from 1060 to 3000 Hz for the suction side, and from 700 to 520 Hz for the pressure side. The frequency and wavenumber ranges are obtained by using a database method [56, 57]. The data is generated using both Falkner–Skan–Cooke (FSC) similar profiles and outputs from our LST code. For each wave, the modes obtained from the database method are analyzed in our LST framework to determine the neutral point locations. For flight condition 2, however, the transition on the lower airfoil side is found to be caused by an LSB, differing from all the other situations in which the amplification of TS waves triggers transition to turbulence. The base flows used here are obtained from our conical boundary layer code. The C_p distribution from an initially fully turbulent run is used as the boundary condition for the boundary layer solver. Figure 6 shows the N-envelopes for both flight conditions. For flight condition 2, the N-envelope is not shown for the pressure side, since transition takes place by means of an LSB for this case.

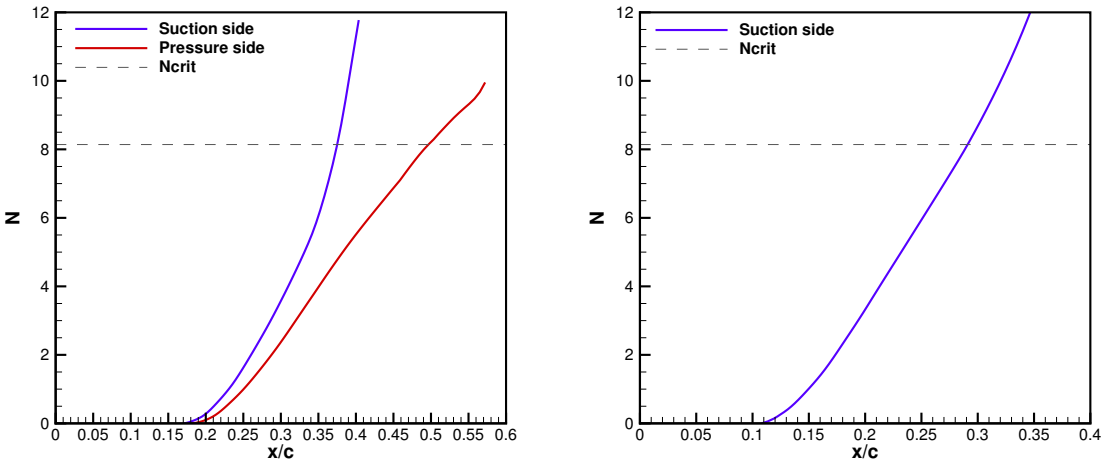

(a) Flight condition 1

(b) Flight condition 2

Figure 6: N-factor envelopes for condition 1 (left) and condition 2 (right) for the NLF(1)-0416 test case.

Table 4 lists the numerical and experimental transition locations for this test case.

Table 4: NLF(1)-0416 airfoil transition points.

Condition	Side	PSE, $(x/c)_{tr}$	Experiment, $(x/c)_{tr}$ [29]	Difference (%)
1	Upper	0.375	0.385	2.56
1	Lower	0.497	0.525	5.34
2	Upper	0.291	0.310	6.03
2	Lower	0.570	0.640	10.85

The experimental transition locations reported by Somers [29] are obtained through the use of acoustic devices that do not precisely detect transition. Instead, this method

suggests bounds inside which transition takes place. Then, a curve is fitted, passing inside the bounding regions, to indicate the likely transition location. The experimental results shown in Table 4 are based on this curve. This approach certainly inputs some additional uncertainty on the transition location placing. Despite the uncertainties involved with the experimental transition location, the results provided by our PSE implementation are in good agreement with experimental data.

The critical N-factor that leads to the computed transition location being the same as in the experiments is $N_{\text{crit,TS}} = 9.3$, corresponding to a freestream turbulence value of $Tu = 0.106\%$ according to Eq. (25). Once again, we consider the uncertainties present in the experimental transition location determination and, therefore, advise using $N_{\text{crit,TS}} = 8.14$ for low-turbulence wind tunnels unless a precise value of turbulence level is available.

For the airfoil pressure side in flight condition 2, the larger mismatch between numerical and experimental result follows the trend typical of linear stability analysis tools, which is to tend to predict transition caused by LSBs upstream of its experimental location. Indeed, the way a separation bubble is accounted for in this type of framework involves the boundary layer code divergence. Boundary layer computations involve a numerical marching scheme, and hence they represent a parabolic problem whose underlying hypotheses are similar to the ones considered for the PSE approach. When the flow separates, the slow streamwise variation hypothesis does not hold, and the marching procedure diverges. The correlations reported by Shi et al. [48] provide a tool to estimate the transition region when separation is involved.

5 Transitional Flow Results in a Discontinuous Galerkin RANS framework

We propose to use PSE as the transition location prediction tool in a DG RANS framework. This framework is such that the advantages of a low-dissipation, adaptive CFD method are used to simulate transitional flows at high Reynolds numbers, in contrast to techniques such as ILES, which are restricted to low to moderate Reynolds numbers. In the numerical simulations, we use DG with approximation order $p = 2$ on meshes adapted via adjoint-based output error estimates. An unstructured mesh optimization algorithm through error sampling and error synthesis (MOESS) is adopted to capture the highly anisotropic physics in the boundary layer with a moderate number of degrees of freedom (DOF). In this paper, our meshes are adapted for the drag output only, given that this is the aerodynamic coefficient most affected by including the transition model. Since the transition changes the system of equations in the CFD code, the error estimation and mesh adaptation also include the transition model.

5.1 NACA 0012

To first verify the concepts presented in Sec. 3, we use the NACA 0012 airfoil results presented in Sec. 4 with Reynolds numbers of 5 and 15 million, for $M = 0.1$ and zero angle of attack. The starting and final computational meshes are shown in Fig. 7,

where 25 mesh optimization iterations were required to obtain the final computational mesh.

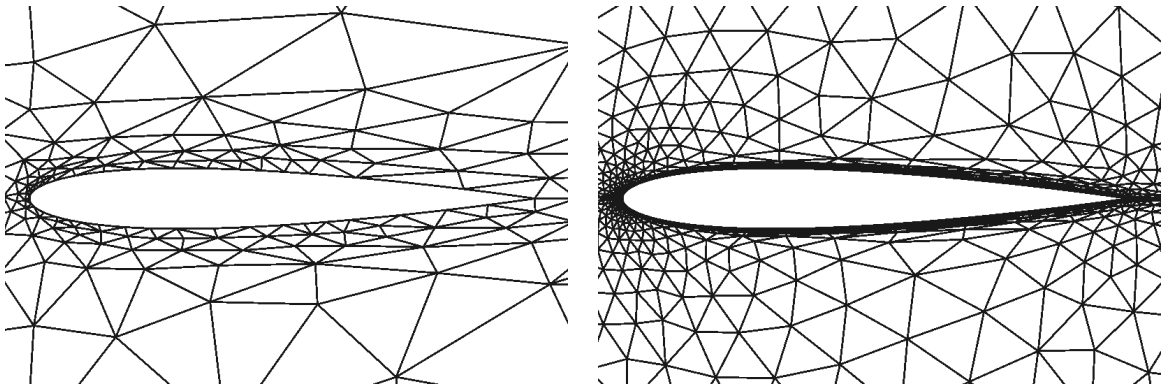

(a) Initial mesh. DOF = 3198 (b) Adapted mesh. DOF = 41190

Figure 7: Examples of initial and adapted meshes for a NACA 0012 simulation.

Figure 8 shows contours of $\tilde{\nu}$, which is the SA model working variable and is directly related to the kinetic eddy viscosity. Both fully turbulent and transition computations are shown for the 5 million Reynolds number are shown. It is evident that our implementation is able to turn off the turbulence effects upstream of the transition region. After this position, predicted by PSE, the intermittency function from Eq. (26) is used to turn on the turbulence production and destruction terms.

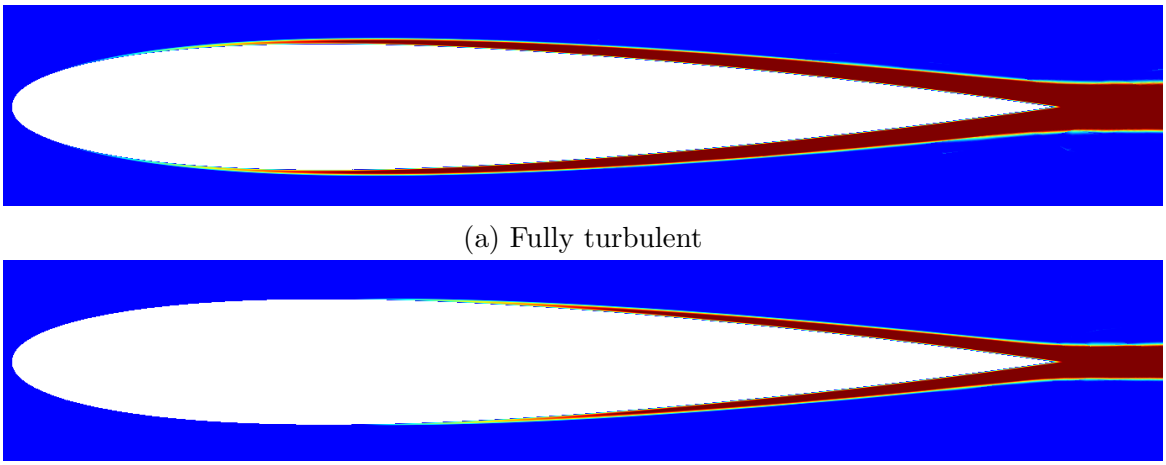

(a) Fully turbulent

(b) Transition included

Figure 8: SA model working variable $\tilde{\nu}$ contours for the NACA 0012 airfoil at $Re =$ 5 million for a fully-turbulent simulation (top) and including transitional modeling (bottom). The contour range is from 0 to 0.02.

The effects of transition on the pressure coefficient distribution are shown in Fig. 9. The overall C_p distribution looks similar for both turbulent and transitional test cases, which seems to be physical since no shock waves are present in this case. By looking at

the C_p curve around the transition region in detail, however, we see that the transitional flow case presents small differences compared to the turbulent case.

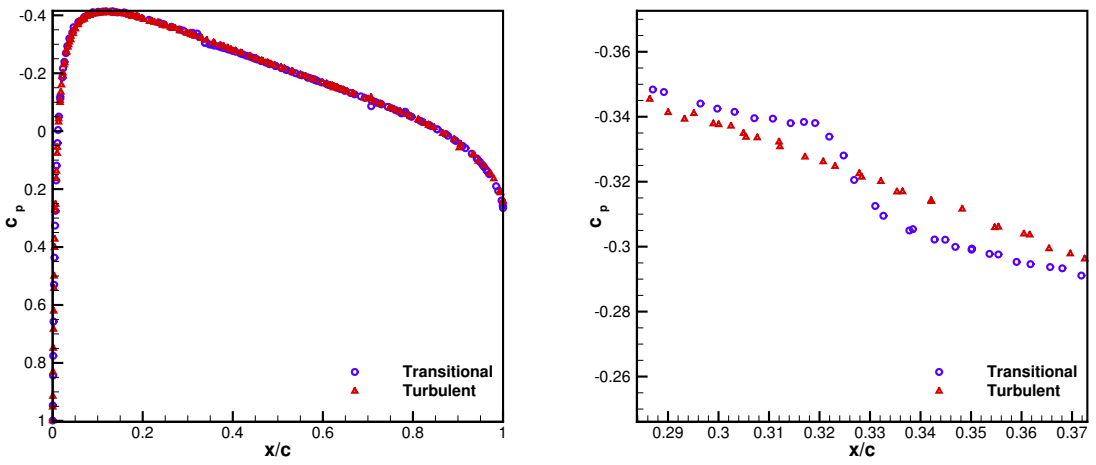

(a) C_p, overview

(b) C_p, zoom-in around the transition region

Figure 9: Pressure coefficient distributions. General view (left) and zoomed-in image around the transition region (right) for the NACA 0012 case with Re=5 million.

To better analyze the transition location for the NACA 0012 upper surface at $Re = 5$ million, we look at the skin friction coefficient, C_f, plots for both fully-turbulent and transitional simulations. The results are shown on the left of Fig. 10. The inclusion of a laminar region, followed by a transitional length in the simulation leads to a smaller skin friction coefficient, as expected. In addition, the fact that C_f rises around $(x/c) = 0.3$ is another indication that the transition predicted to start at $(x/c) = 0.33$ by our PSE approach, is being correctly reproduced within the RANS framework. Inspection of the skin friction plot shows that some points seem to be off the curve. This is likely due to the discontinuous approximation in the DG approach.

In Fig. 10 we also show the streamwise velocity component, U, at three different chord-wise positions for the transitional flow case. First, the velocity profile in the laminar region is representative of laminar flow. As long as turbulence starts being generated in the boundary layer, the enlarged momentum transfer causes the boundary layer velocity profile to become flatter, as we show in Fig. 10. The relevance of these analyses is that we assure that the interaction between the transition prediction framework and the CFD capability is such that the physical aspects of laminar, transitional, and turbulent flows are retained in the simulation.

The values for lift, drag, and moment coefficient (about $c/4$) are listed in Table 5 for both flight conditions (Reynolds numbers of 5 and 15 million).

By including transition effects, the drag is lower by 30% for the 5 million Reynolds case and by 20% in the 15 million Reynolds case. As for the lift coefficient, the larger variation is observed for the lower Reynolds number case. Since the NACA 0012 airfoil is symmetric and we use a zero angle of attack condition, both lift and moment coefficients are small numbers, and thus, it is harder to draw meaningful conclusions

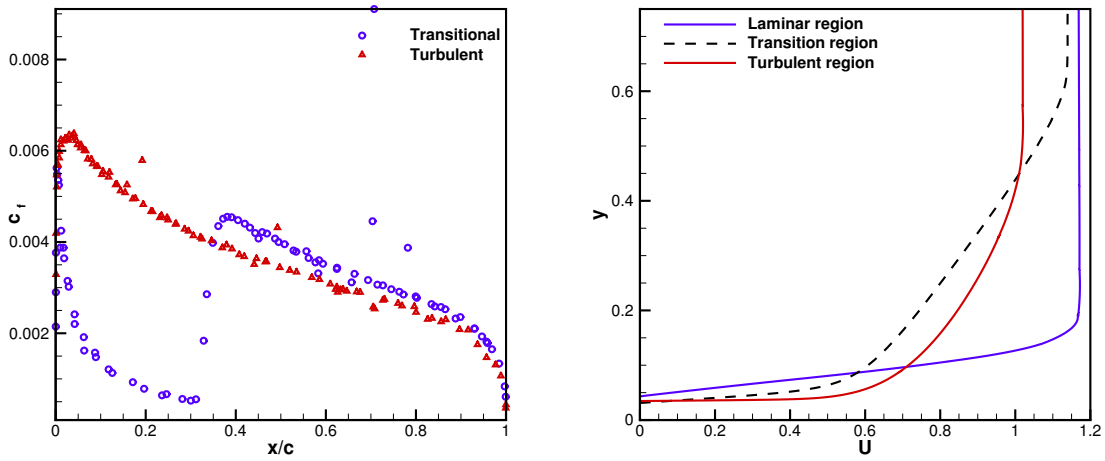

(a) C_f (b) U, transitional flow

Figure 10: NACA 0012 skin friction coefficient for both turbulent and transitional simulations (left) and streamwise velocity in the laminar, transitional, and turbulent regions for the transitional simulation (right) for $Re = 5$ million.

Table 5: NACA 0012 aerodynamic coefficients

Re (million)	BL type	c_l	c_d	c_m
5	Turbulent	−0.000922	0.00864	0.000189
5	Transitional	−0.000438	0.00602	0.000129
15	Turbulent	−0.000851	0.00749	0.000154
15	Transitional	0.000847	0.00603	0.000165

about the effect of transition on these variables.

5.2 NLF(1)-0416

Since a considerable amount of experimental data is available for the NLF(1)-0416 airfoil, we use flight condition 1 ($Re = 4$ million, $M = 0.1$, and zero angle of attack) and condition 2 ($Re = 2$ million, $M = 0.1$, and 4° angle of attack) from Sec. 4 to assess both the fully-turbulent and transitional flows for this specific geometry. The starting and final computational meshes are visualized in Fig. 11. We start with a coarse mesh and, as the drag error estimates are performed, our mesh adaptation algorithm refines regions in a way that the numerical error in the drag calculation is minimized.

Figure 12 shows contours of $\tilde{\nu}$ for condition 1 for both fully turbulent and including transition to turbulence simulations. Here, for a non-symmetric, thicker than the NACA 0012 airfoil, it is even easier to observe the intermittency function effects over the SA model turbulent variables.

The pressure coefficient distributions for the turbulent simulation, the transitional simulation, and the experimental data are shown in Fig. 13. Both fully-turbulent and transitional flow simulations show a good agreement with the experimental C_p

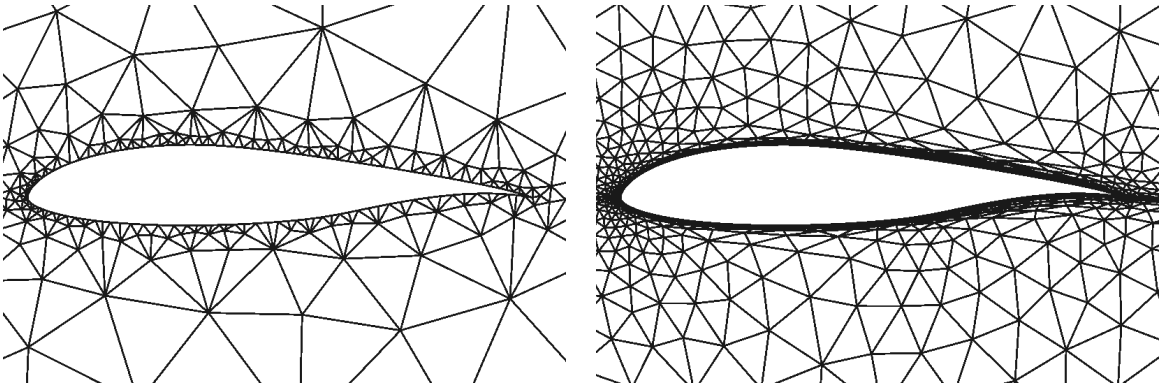

(a) Initial mesh. DOF = 3,516 (b) Adapted mesh. DOF = 41,484

Figure 11: Examples of initial and adapted meshes for a NLF(1)-0416 run.

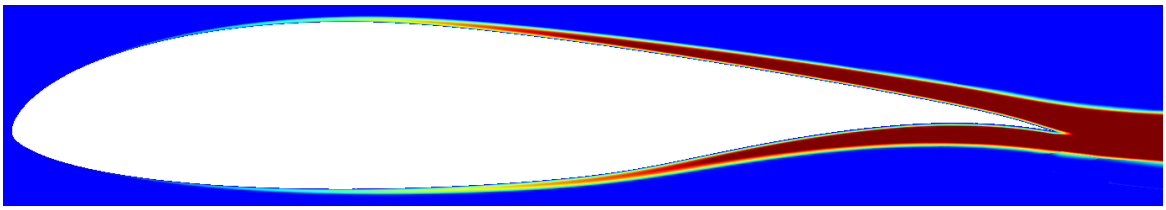

(a) Fully turbulent

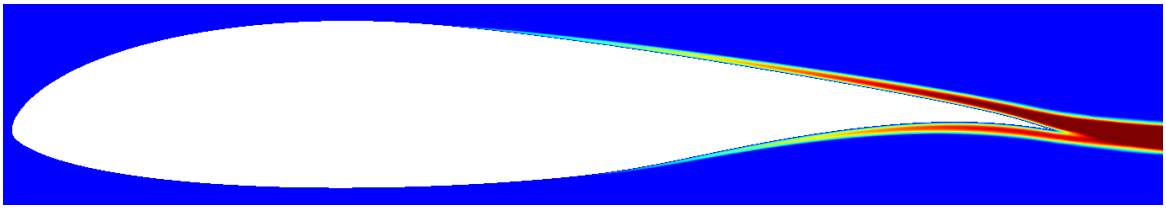

(b) Transition included

Figure 12: SA model working variable $\tilde{\nu}$ contours for the NLF(1)-0416 case at $Re = 4$ million for a fully turbulent simulation (top) and including transitional effects (bottom). The contour range is from 0 to 0.03.

distribution. However, we observe some disagreement close to the transition region if a turbulent run is performed. The more significant mismatches in the pressure coefficient curve are observed inside the transition region for the airfoil suction side. At $(x/c) = 0.4$, that is inside the transition region, the error in the pressure coefficient for the fully-turbulent run is of 9%. When transition to turbulence effects are included, the error drops to 3.7%. On the airfoil pressure side, the fully-turbulent simulation leads to better agreement with experimental data, the transitional flow run leading to better agreement in the suction side. Once again, the upper surface transition region inspection, predicted to take place between $(x/c) = 0.375$ and $(x/c) = 0.446$, introduces features that are representative of the experimental pressure coefficient distribution, namely a small step increase in the C_p values around the transition region.

Figure 14 shows the skin friction coefficient, C_f, for both turbulent and transitional simulations. Besides the larger C_f values for the turbulent case, as expected, the C_f

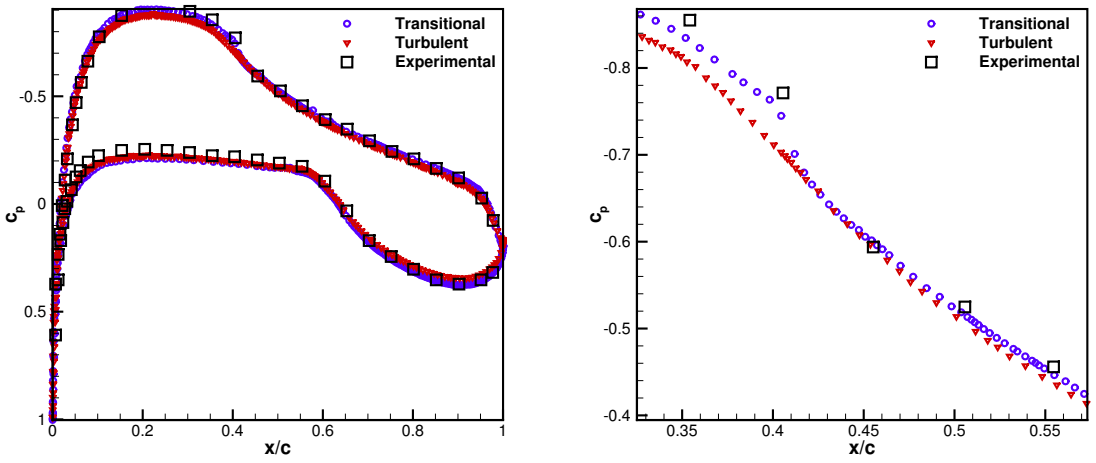

(a) C_p, overview (b) C_p, zoom-in around the transition region

Figure 13: Pressure coefficient distributions. Overall view (left) and detailed view around the suction side transition region (right) for flight condition 1, NLF(1)-0416.

computations vary between turbulent and transitional analyses, even in the turbulent region. This is a result from the boundary layer convection, which introduces history effects in this type of flow, and is correctly captured by the simulations. As a result, the turbulent boundary layer, which was laminar in the early chord positions, has a development that is distinct from the one observed in the fully-turbulent case.

Figure 14 also shows the streamwise velocity plots for the upper surface, in condition 1, for the laminar, transitional, and turbulent regions. As for the NACA 0012 case, we observe that our implementation computes boundary layer velocity profiles that are in agreement with the expectation of an increased momentum transfer leading to flatter velocity profiles in the turbulent flow regime.

Table 6 lists the aerodynamic coefficients for transitional and turbulent simulations and compares them to the experimental data. By including transition to turbulence effects, the error in the drag coefficient prediction drops by one order of magnitude when compared to the fully-turbulent test case. The lift coefficient is overpredicted by the transitional simulations. This trend was also observed by Coder [50]. For the L/D ratio, the transitional simulations reproduce the experimental value more closely, even though the error is still considerable due to the overprediction of the lift coefficient when transitional effects are included. The moment coefficient around the quarter chord exhibits similar errors for both turbulent and transitional analyses.

Table 6: NLF(1)-0416 aerodynamic coefficients for condition 1.

Case	c_l	$\Delta_{c_l}, \%$	c_d	$\Delta_{c_d}, \%$	L/D	$\Delta_{L/D}, \%$	c_m	$\Delta_{c_m}, \%$
Turbulent	0.450	0.75	0.0099	68.65	45.26	40.26	−0.0995	4.36
Transitional	0.486	8.86	0.0055	6.18	87.91	16.03	−0.1080	3.75
Experiment	0.447	–	0.0059	–	75.76	–	−0.1040	–

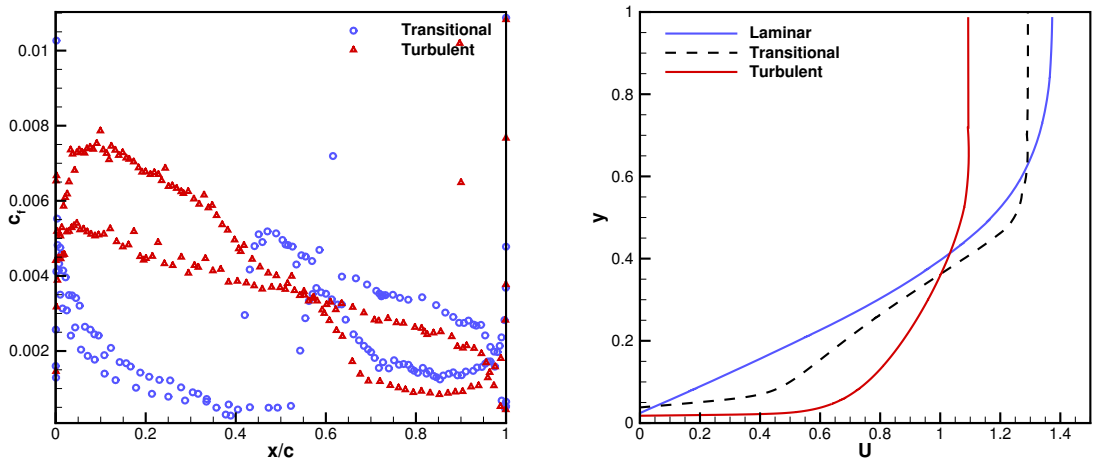

(a) C_f (b) U, transitional flow. Suction side

Figure 14: NLF(1)-0416 skin friction coefficient for both turbulent and transitional simulations (left) and streamwise velocity in the laminar, transitional, and turbulent regions for the transitional simulation (right) for the suction side at $Re = 4$ million, $M = 0.1$, and zero angle of attack (condition 1).

Figure 15 shows $\tilde{\nu}$ contours for condition 2 ($Re = 2$ million, $M = 0.1$, and 4° angle of attack) for both fully turbulent and transition simulations. The intermittency function effects over the turbulence variables are once again present. At a higher angle of attack, condition 2 is the best condition (among the ones addressed in this paper) to visualize the differences in the $\tilde{\nu}$ contours between both transitional and turbulent cases.

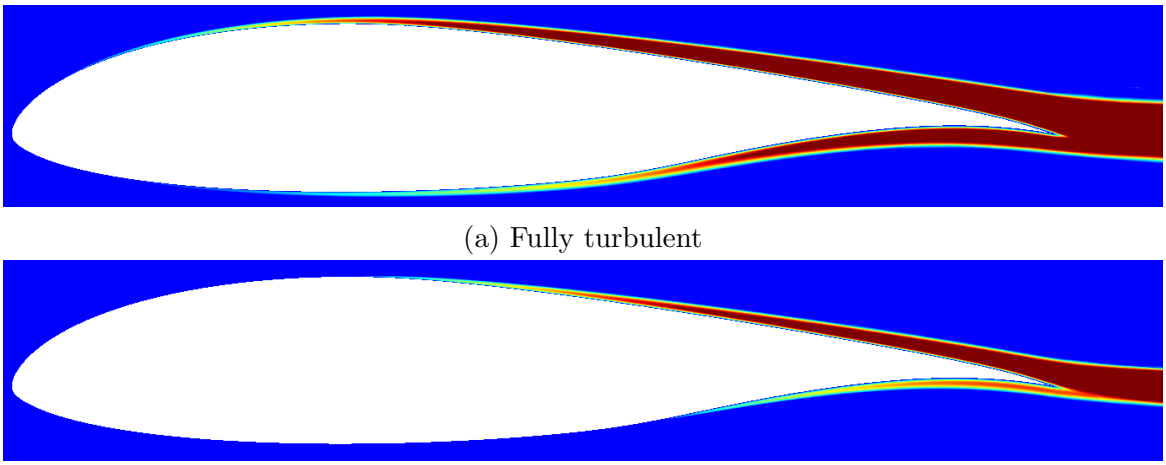

(a) Fully turbulent

(b) Transition included

Figure 15: SA model working variable $\tilde{\nu}$ contours for the NLF(1)-0416 case at $Re = 2$ million for a fully turbulent simulation (top) and including transitional effects (bottom). The contour range is from 0 to 0.03.

The C_p distributions for both turbulent and transitional simulations are shown in Fig. 16. In contrast to flight condition 1, there is no experimental data available for the C_p distribution corresponding to flight condition 2. For flight condition 2, the differences in the C_p curves as obtained by turbulent and transitional simulations are more clearly noticeable than for flight condition 1, especially close to the suction peak. On the pressure side with transition, a separation region is partially detected by the simulation close to $(x/c) = 0.6$. This is represented by the fast C_p drop in the aforementioned chord position. This separation is not captured by the fully turbulent simulation. This is consistent with the fact that turbulent boundary layers are more resistant to separation than laminar ones.

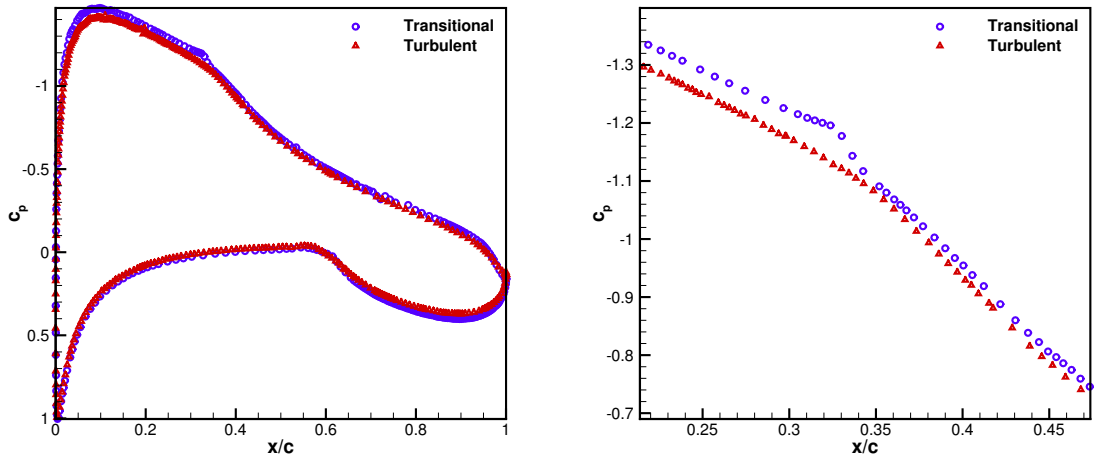

(a) C_p, overview (b) C_p, zoom-in around the transition region

Figure 16: C_p distributions. Overall view (left) and detailed view around the suction side transition region (right) for flight condition 2, NLF(1)-0416.

Figure 17 shows the skin friction coefficient, C_f, for both turbulent and transitional simulations. The C_f value that is close to zero around $(x/c) = 0.6$ correlates well with the laminar separation bubble that triggers transition in the experimental framework, which is consistent with Fig. 16. Once again, the velocity profiles shown in Fig. 17 clearly distinguish between laminar, transitional, and turbulent flow regions on the airfoil suction side.

Table 7 lists the aerodynamic coefficients for the transitional and turbulent simulations and compares them to the experimental data. For flight condition 2, the inclusion of transition to turbulence effects improves the drag coefficient prediction, as well as the L/D computation, leading to results that are close to experimental data. The inclusion of transition to turbulence effects reduces the error in L/D from 37% for the fully-turbulent case to 8% in the transitional one. The lift coefficient, however, is once more overpredicted by the inclusion of transition to turbulence modeling.

The NLF(1)-0416 experimental results might suffer from wall effects in the wind tunnel facility and our numerical results do not account for this. Also, there is no experimental information regarding the transition front in different spanwise locations.

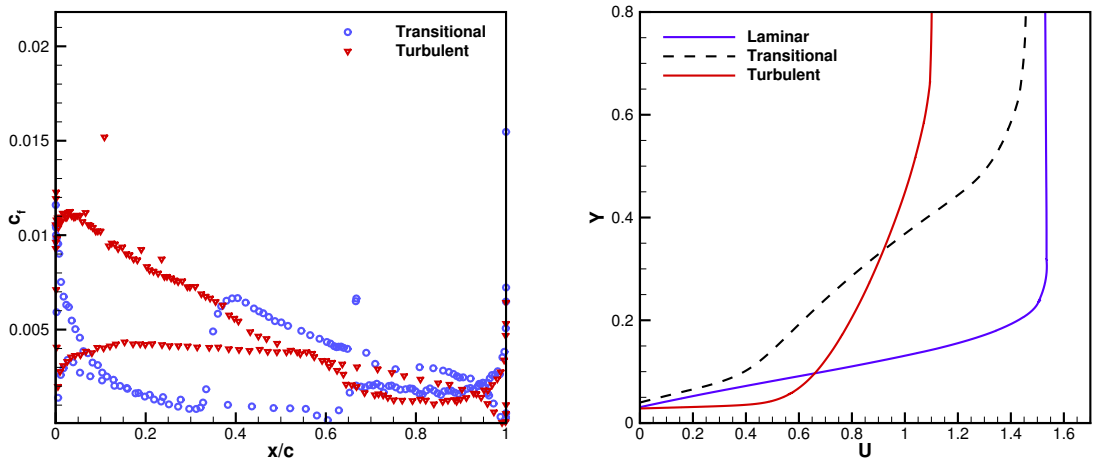

(a) C_f (b) U, transitional flow. Suction side

Figure 17: NLF(1)-0416 skin friction coefficient for both turbulent and transitional simulations (left) and streamwise velocity in the laminar, transitional, and turbulent regions for the transitional simulation (right) for the suction side at 4 million, $M = 0.1$, and 4° angle of attack (condition 2).

Table 7: NLF(1)-0416 aerodynamic coefficients for condition 2.

Case	c_l	$\Delta_{c_l}, \%$	c_d	$\Delta_{c_d}, \%$	L/D	$\Delta_{L/D}, \%$	c_m	$\Delta_{c_m}, \%$
Turbulent	0.889	1.07	0.0126	61.09	70.79	37.26	−0.0999	0.11
Transitional	0.937	6.53	0.0077	1.56	122.09	8.21	−0.1090	9.19
Experiment	0.880	–	0.0078	–	112.82	–	−0.1000	–

Checking this point is relevant to ensure that the experimental results are not subject to three-dimensional effects.

6 Conclusions

We successfully demonstrate that the inclusion of transition to turbulence modeling in a RANS framework improves the agreement with experimental data. Our approach is unique in that it introduces laminar and transitional flow areas in a CFD code that uses a DG discretization and goal-adapted mesh refinement. The fact that both nonlocal and nonparallel effects are included in the transition module results in accurate prediction of transition in boundary layer flows. The framework is targeted at solving high-Reynolds number transitional aerodynamic flows.

The main advantage of the PSE method with respect to local stability analysis tools is that it accounts for the boundary layer growth. In the PSE method, base flow gradients in the wall normal direction are stronger than in the streamwise direction. Our PSE implementation is verified by comparing to another code, NOLOT [20], which is considered a mature PSE implementation. The kinetic energy-based growth rates

are compared to those obtained with NOLOT. This is done for both subsonic and supersonic flows over flat plates, considering oblique and aligned TS waves. Two airfoil test cases are also considered. Transition results for a NACA 0012 case at different Reynolds numbers, as well as for the NLF(1)-0416 airfoil, demonstrate that our PSE framework correctly predicts transition triggered by amplification of TS waves. Experimental results are also used for validation purposes. We compare numerical results for aerodynamic coefficients from fully-turbulent and transitional simulations with those from experimental data for the NLF(1)-0416 airfoil. For the 4 million Reynolds number flight condition, we observe that including transition effects in the numerical simulations leads to a drag coefficient error of 6.2%, against 68.7% when a fully-turbulent simulation is performed. For the 2 million Reynolds number flight condition, the transitional simulation gives a drag coefficient error of 1.6%, compared to 61.1% for the fully-turbulent case.

We are able to turn off production and destruction turbulence terms in the SA turbulence model by using a continuous, smooth intermittency function. By doing so, transition to turbulence effects are accounted for in a RANS framework. We demonstrate that, by including transition to turbulence in our RANS, high order framework, the drag coefficient becomes more accurate compared to the fully-turbulent model. The lift coefficient tends to be overpredicted when the transition model is included, but L/D becomes better correlated to experimental data.

The main motivation for including laminar-turbulent transition effects in current CFD simulations is the quest for designing lower drag airframes. In addition, transition affects other aerodynamic forces and characteristics, which impacts not only aerodynamics, but overall performance, and flight mechanics as well. In that sense, using an adaptive high-order RANS framework along with a PSE-based transition capability paves the way for higher-fidelity multidisciplinary design and optimization.

Acknowledgments

The authors gratefully acknowledge the support provided by Conselho Nacional de Desenvolvimento Científico e Tecnológico, CNPq, Brazil, under Research Grant No. 205552/2014-5. The authors also thank Prof. Ardeshir Hanifi (KTH) for the insightful discussions on the PSE approach.

References

[1] Crouch, J. D., and Ng, L. L., "Variable N-Factor Method for Transition Prediction in Three-Dimensional Boundary Layers," *AIAA Journal*, Vol. 38, No. 2, 2000, pp. 211–216. doi:10.2514/2.973.

[2] Arnal, D., "Practical Transition Prediction Methods: Subsonic and Transonic Flows," Advances in Laminar Turbulent Transition Modeling. The Lecture Series of the von Karman Institute, 2008.

[3] Deyhle, H., and Bippes, H., "Disturbance Growth in an Unstable

Three-Dimensional Boundary Layer and its Dependence on Environmental Conditions," *Journal of Fluid Mechanics*, Vol. 316, 1996, pp. 73–113. doi:10.1017/S0022112096000456.

[4] Lynde, M. N., and Campbell, R. L., "Computational Design and Analysis of a Transonic Natural Laminar Flow Wing for a Wind Tunnel Model," AIAA Paper No. 2017-3058*, Proceedings of the 35th AIAA Applied Aerodynamics Conference, AIAA AVIATION Forum*, Denver, CO, 2017. doi:10.2514/6.2017-3058.

[5] Gaster, M., and Jiang, F., "A Rapid Scheme for Estimating Transition on Wings by Linear Stability Theory," *Proceedings of the 19th Congress of the International Council of Aeronautical Sciences*, 1994.

[6] van Ingen, J. L., "Some Introductory Remarks on Transition prediction Methods based on Linear Stability Theory," *Proceedings of the colloquium Transitional Boundary Layers in Aeronautics*, R. A. W. M. Henkes and J. L. van Ingen ed., Amsterdam, 1996.

[7] Stock, H., and Haase, W., "Some Aspects of Linear Stability Calculations in Industrial Applications," *Proceedings of the colloquium Transitional Boundary Layers in Aeronautics*, R. A. W. M. Henkes and J. L. van Ingen ed., Amsterdam, 1996.

[8] Crouch, J. D., Crouch, I. W. M., and Ng, L. L., "Transition Prediction for Three-Dimensional Boundary Layers in Computational Fluid Dynamics Applications," *AIAA Journal*, Vol. 40, No. 8, 2002, pp. 1536–1541. doi:10.2514/2.1850.

[9] Drela, M., "Implicit Implementation of the Full eN Transition Criterion," AIAA Paper No. 2003-4066*, Proceedings of the 21st AIAA Aplied Aerodynamics Conference*, Orlando, FL, 2003. doi:10.2514/6.2003-4066.

[10] Halila, G. L. O., Bigarella, E. D. V., and Azevedo, J. L. F., "A Numerical Study on Transitional Flows Using a Correlation-Based Transition Model," *Journal of Aircraft*, Vol. 53, No. 4, 2016, pp. 922–941. doi:10.2514/1.C033311.

[11] Halila, G. L. O., Bigarella, E. D. V., Antunes, A. P., and Azevedo, J. L. F., "An Efficient Setup for Freestream Turbulence on Transition Prediction over Aerospace Configurations," *Aerospace Science and Technology*, Vol. 81, 2018, pp. 259–271. doi:10.1016/j.ast.2018.08.013.

[12] Pasquale, D., Rona, A., and Garret, S. J., "A Selective Review of CFD Transition Models," AIAA Paper No. 2009-3812*, Proceedings of the 39th AIAA Fluid Dynamics Conference*, San Antonio, TX, 2009. doi:10.2514/6.2009-3812.

[13] Fernandez, P., Nguyen, N., and Peraire, J., "The Hybridized Discontinuous Galerkin Method for Implicit Large-Eddy Simulation of Transitional Turbulent Flows," *Journal of Computational Physics*, Vol. 336, 2017, pp. 308–329. doi:10.1016/j.jcp.2017.02.015.

[14] Uranga, A., Persson, P. O., Drela, M., and Peraire, J., "Implicit Large Eddy Simulation of Transition to Turbulence at low Reynolds Numbers using a Discontinuous Galerkin Method," *International Journal for Numerical Methods in Engineering*, Vol. 87, 2010, pp. 232–261. doi:10.1002/nme.3036.

[15] Zheng, X., Liu, C., and Yang, C., "Turbulent Transition Simulation Using the $k-\omega$ Model," *International Journal for Numerical Methods in Engineering*, Vol. 42, 1998, pp. 907–926.

[16] Juniper, M. P., Hanifi, A., and Theofilis, V., "Modal Stability Theory. Lecture notes from the FLOW-NORDITA Summer School on Advanced Instability Methods for Complex Flows. Stockholm, Sweden, 2013," *Aplied Mechanics Reviews*, Vol. 66, 2014, pp. 1–22. doi:10.1115/1.4026604.

[17] Saric, W. S., "Introduction to Linear Stability," Advances in Laminar Turbulent Transition Modeling. The Lecture Series of the von Karman Institute, 2008.

[18] Saric, W. S., and Nayfeh, A. H., "Nonparallel Stability of Boundary–Layer Flows," *Physics of Fluids*, Vol. 18, 1975, pp. 945–950. doi:10.1063/1.861266.

[19] Crighton, D. G., and Gaster, M., "Stability of Slowly Diverging Jet Flow," *Journal of Fluid Mechanics*, Vol. 77, 1976, pp. 397–413. doi:10.1017/S0022112076002176.

[20] Hanifi, A., Henningson, D., Hein, S., Bertolotti, F., and Simen, M., "Linear Nonlocal Instability Analysis - the linear NOLOT code," The aeronautical research institute of sweden aerodynamics department, FFA-TN 1994-54, 1994.

[21] El-Hady, N. M., "Nonparallel Instability of Supersonic and Hypersonic Boundary Layers," *Physics of Fluids A: Fluid Dynamics*, Vol. 3, 1991, pp. 2164–2178. doi:10.1063/1.857898.

[22] Herbert, T., "Parabolized Stability Equations," *Annual Review of Fluid Mechanics*, Vol. 29, 1997, pp. 245–283. doi:10.1146/annurev.fluid.29.1.245.

[23] Schmid, P., and Henningson, P., *Stability and Transition in Shear Flows*, Springer, New York, 2001. doi:10.1007/978-1-4613-0185-1.

[24] Bertolotti, F. P., and Herbert, T., "Analysis of the Linear Stability of Compressible Boundary Layers using PSE," *Theoretical and Computational Fluid Dynamics*, , No. 3, 1991, pp. 117–124. doi:10.1007/BF00271620.

[25] Bertolotti, F. P., Herbert, T., and Spalart, P. R., "Linear and Nonlinear Stability of the Blasius Boundary Layer," *Journal of Fluid Mechanics*, Vol. 242, 1992, pp. 441–474. doi:10.1017/S0022112092002453.

[26] Kosarev, L., Séror, S., and Lifshitz, Y., "Parabolized Stability Equations Code with Automatic Inflow for Swept Wing Transition Analysis," *Journal of Aircraft*, Vol. 53, No. 6, 2016, pp. 1647–1669. doi:10.2514/1.C033509.

[27] Arnal, D., "Boundary layer Transition: Predictions based on the Linear Theory," AGARD Report AG 793, Apr. 1994.

[28] van Ingen, J. L., "A Suggested Semi-Empirical Method for the Calculation of the Boundary Layer Transition Region," Univ. Delft Report VTH-74, University of Delft, Delft, The Nederlands, 1956.

[29] Somers, D. M., "Design and Experimental Results for a Natural-Laminar-Flow Airfoilfor General Aviation Applications," NASA TP-1981-1861, NASA, Jun. 1981.

[30] Allmaras, S. R., and Johnson, F. T., "Modifications and Clarifications for the Implementation of the Spalart-Allmaras Turbulence Model," *Seventh International Conference on Computational Fluid Dynamics (ICCFD7)*, 2012, pp. 1–11.

[31] Baumann, C. E., and Oden, J. T., "A Discontinuous hp Finite Element Method for Convection-diffusion Problems," *Computer Methods in Applied Mechanics and Engineering*, Vol. 175, No. 3, 1999, pp. 311 – 341. doi:10.1016/S0045-7825(98)00359-4, URL http://www.sciencedirect.com/science/article/pii/S0045782598003594.

[32] Houston, P., and Süli, E., "HP-adaptive Discontinuous Galerkin Finite Element Methods for First-Order Hyperbolic Problems," *SIAM Journal on Scientific Computing*, Vol. 23, No. 4, 2001, pp. 1226–1252. doi:10.1137/S1064827500378799.

[33] Wang, L., and Mavriplis, D. J., "Adjoint-based h-p Adaptive Discontinuous Galerkin Methods for the 2D Compressible Euler Equations," *Journal of Computational Physics*, Vol. 228, No. 20, 2009, pp. 7643 – 7661. doi:10.1016/j.jcp.2009.07.012, URL http://www.sciencedirect.com/science/article/pii/S0021999109003854.

[34] Roe, P. L., "Approximate Riemann Solvers, Parameter Vectors, and Difference Schemes," *Journal of Computational Physics*, Vol. 43, No. 2, 1981, pp. 357–372. doi:10.1016/0021-9991(81)90128-5.

[35] Bassi, F., and Rebay, S., "GMRES Discontinuous Galerkin Solution of the Compressible Navier-Stokes Equations," *Discontinuous Galerkin Methods*, Springer, 2000, pp. 197–208. doi:10.1007/978-3-642-59721-3_14.

[36] Wang, Z., Fidkowski, K., Abgrall, R., Bassi, F., Caraeni, D., Cary, A., Deconinck, H., Hartmann, R., Hillewaert, K., Huynh, H., Kroll, N., May, G., Persson, P.-O., van Leer, B., and Visbal, M., "High-Order CFD Methods: Current Status and Perspective," *International Journal for Numerical Methods in Fluids*, 2013. doi:10.1002/fld.3767.

[37] Hartmann, R., and Houston, P., "Adaptive Discontinuous Galerkin Finite Element Methods for the Compressible Euler Equations," *Journal of Computational Physics*, Vol. 183, No. 2, 2002, pp. 508–532. doi:10.1006/jcph.2002.7206.

[38] Venditti, D. A., and Darmofal, D. L., "Grid Ddaptation for Functional Outputs: Application to Two-Dimensional Inviscid Flows," *Journal of Computational Physics*, Vol. 176, No. 1, 2002, pp. 40–69. doi:10.1006/jcph.2001.6967.

[39] Fidkowski, K. J., and Darmofal, D. L., "Review of Output-Based Error Estimation and Mesh Adaptation in Computational Fluid Dynamics," *AIAA journal*, Vol. 49, No. 4, 2011, pp. 673–694. doi:10.2514/1.J050073.

[40] Yano, M., and Darmofal, D. L., "An Optimization-based Framework for Anisotropic Simplex Mesh Adaptation," *Journal of Computational Physics*, Vol. 231, No. 22, 2012, pp. 7626–7649. doi:10.1016/j.jcp.2012.06.040.

[41] Fidkowski, K., "A Local Sampling Approach to Anisotropic Metric-based Mesh Optimization," *54th AIAA Aerospace Sciences Meeting*, 2016, p. 0835. doi:10.2514/6.2016-0835.

[42] White, F. M., *Viscous Fluid Flow*, McGraw-Hill, New York, NY, 1991.

[43] Bertolotti, F. P., *Turbulence and Transition Modelling. Ch. 8, Transition Modelling based on the PSE*, Kluwer Academic Publishers, Netherlands, 1996.

[44] Andersson, P., Henningson, D. S., and Hanifi, A., "On a Stabilization Procedure for the Parabolic Stability Equations," *Journal of Engineering Mathematics*, Vol. 33, 1998, pp. 311–332. doi:10.1023/A:1004367704897.

[45] Chang, C. L., "LASTRAC.3d: Transition Prediction in 3D Boundary Layers," AIAA Paper No. 2004-2542*, Proceedings of the 34th AIAA Fluid Dynamics Conference and Exhibit*, Portland, OR, 2004. doi:10.2514/6.2004-2542.

[46] Langlois, M., Casalis, G., and Arnal, D., "On the Practical Applications of the PSE Approach to Linear Stability Analysis," *Aerospace Science and Technology*, Vol. 2, No. 3, 1998, pp. 167–176. doi:10.1016/S1270-9638(98)80051-5.

[47] Mack, L. M., "Transition Prediction and Linear Stability Theory," AGARD Report CP224, 1977.

[48] Shi, Y., Gross, R., Mader, C. A., and Martins, J. R. R. A., "Transition Prediction in a RANS Solver based on Linear Stability Theory for Complex Three-Dimensional Configurations," *Proceedings of the AIAA Aerospace Sciences Meeting, AIAA SciTech Forum*, Kissimmee, FL, 2018. doi:10.2514/6.2018-0819.

[49] Krumbein, A., "Automatic Transition Prediction and Application to Three-Dimensional Wing Configurations," *Journal of Aircraft*, Vol. 44, No. 1, 2007, pp. 119–133. doi:10.2514/1.22254.

[50] Coder, J. G., *Development of a CFD-compatible Transition Model based on Linear Stability Theory*, Ph.D. Thesis, The Pennsylvania State Univeristy, State College, PA, 2014.

[51] Langtry, R. B., and Menter, F. R., "Correlation-Based Transition Modeling for Unstructured Parallelized Computational Fluid Dynamics Codes," *AIAA Journal*, Vol. 47, No. 12, 2009, pp. 2894–2906. doi:10.2514/1.42362.

[52] Drela, M., "Low-Reynolds Number Airfoil Design for the MIT Daedalus Prototype: A Case Study," *Journal of Aircraft*, Vol. 25, No. 8, 1988, pp. 724–732. doi:10.2514/3.45650.

[53] Krumbein, A., Krimmelbein, N., Grabe, C., and Shengyang, N., "Development and Application of Transition Prediction Techniques in an Unstructured CFD code (Invited)," *Proceedings of the AIAA AFluid Dynamics Conference, AIAA Aviation Forum*, Dallas, TX, 2015. doi:10.2514/6.2015-2476.

[54] Shi, Y., Yang, T., Bai, J., Lu, L., and Wang, H., "Research of transition criterion for semi-empirical prediction method at specified transonic regime," *Aerospace Science and Technology*, Vol. 88, 2019, pp. 95–109. doi:10.1016/j.ast.2019.03.012.

[55] von Doenhoff, A. E., and Abbott, F. T., "The Langley Two-Dimensional Low-Turbulence Pressure Tunnel," NACA TN-1947-1283, NACA, May 1947.

[56] Perraud, J., Arnal, D., Casalis, G., Archambaud, J., and Donelli, R., "Automatic Transition Prediction using Simplified Methods," *AIAA Journal*, Vol. 47, No. 11, 2009, pp. 2676–2684. doi:10.2514/1.42990.

[57] Bégou, G., Devinau, H., Vermeersch, O., and Casalis, G., "Database Approach for Laminar-Turbulent Transition Prediction: Navier–Stokes Compatible Reformulation," *AIAA Journal*, Vol. 55, No. 11, 2017, pp. 3648–3660. doi:10.2514/1.J056018.